Applied Surface Science 480 (2019) 1014–1024

Contents lists available at ScienceDirect

Applied Surface Science

journal homepage: www.elsevier.com/locate/apsusc

Full length article

Hydrazine adsorption on perfect and defective fcc nickel (100), (110) and (111) surfaces: A dispersion corrected DFT-D2 study

Elliot S. Menkah[a], Nelson Y. Dzade[b,c,*], Richard Tia[a], Evans Adei[a], Nora H. de Leeuw[b,c]

[a] Theoretical and Computational Chemistry Laboratory, Department of Chemistry, Kwame Nkrumah University of Science and Technology, Kumasi, PMB, Ghana
[b] School of Chemistry, Cardiff University, Main Building, Park PI, Cardiff CF10 3AT, United Kingdom
[c] Department of Earth Sciences, Utrecht University, Princetonplein 8a, 3584 CD Utrecht, Netherlands

ARTICLE INFO

Keywords:
Density functional theory (DFT)
Hydrazine adsorption
Fuel cells
Nickel surfaces

ABSTRACT

We present density functional theory calculations, with a correction for the long-range interactions, of the adsorption of hydrazine (N_2H_4) on the Ni (110), (100), and (111) surfaces, both defect-free planes and surfaces containing point defects in the form of adatoms and vacancies. Several low-energy adsorption structures for hydrazine on the perfect and defective surfaces have been identified and compared. The hydrazine molecule is shown to interact with the Ni surfaces mainly through the lone-pair of electrons located on the N atoms, forming either monodentate or bidentate bonds with the surface. The strength of N_2H_4 adsorption on the perfect surfaces is found to be directly related to their stability, *i.e.* it adsorbs most strongly onto the least stable (110) surface via both N atoms in a *gauche*-bridge configuration ($E_{ads} = -1.43$ eV), followed by adsorption on the (100) where it also binds in gauche-bridge configurations ($E_{ads} = -1.27$ eV), and most weakly onto the most stable (111) surface via one N–Ni bond in a trans-atop configuration ($E_{ads} = -1.18$ eV). The creation of defects in the form of Ni adatoms and vacancies provides lower-coordinated Ni sites, allowing stronger hydrazine adsorption. Analysis into the bonding nature of N_2H_4 onto the Ni surfaces reveals that the adsorption is characterized by strong hybridization between the surface Ni *d*-states and the N *p*-orbitals, which is corroborated by electron density accumulation within the newly formed N–Ni bonding regions.

1. Introduction

The adsorption and reaction of hydrazine (N_2H_4) on metal surfaces has attracted significant attention due to its application in the direct hydrazine fuel cell (DHFC) technology [1,2],. The DHFC technology is a promising alternative for the hydrogen fuel cell, as hydrazine is much easier and cheaper to produce and store than hydrogen. To facilitate the reactions in a fuel cell and produce more electric power from a single cell, stable solid catalysts made of inexpensive materials are necessary. Currently, platinum is the most widely used catalyst in various fuel cells, including for example the proton exchange membrane (PEM) fuel cells [3], due to its stability in the alkaline environment and remarkable catalytic performance, but the high cost and scarcity of platinum-based catalysts severely limit their widespread application in renewable energy conversion systems. Alternative less expensive (transition) metals are therefore urgently needed as electrode catalyst materials in order to make the DHFC technology sustainable. Asazawa et al., have evaluated and compared the fuel cell performances of alternative anode catalyst materials to platinum and found that fuel cell performances in the case of nickel and cobalt are higher than with platinum [4].

Hydrazine adsorption onto the catalyst surface precedes any reactions that take place inside the DHFC, as such, understanding of the strength and features of adsorption of hydrazine onto the metal surface is essential for the successful development of direct hydrazine fuel cells using nickel or other readily available metals as catalyst materials. Detailed atomic-level information regarding the structures and mechanisms of hydrazine adsorption would provide chemical insight into the reactivity of the catalyst, which could be used in the design of improved catalysts. The adsorption energy is one of the important physical quantities that affects the reaction of hydrazine; if the adsorption is energetically favourable, it will lower the activation energy and increase the reaction rate in the anode according to the Arrhenius Eq. [5–7]. An improved reaction rate naturally leads to improvement in the fuel cell power density.

Earlier experimental works have focused mainly on the decomposition reaction of hydrazine into products such as NH_3, NH, N_2H_2, N_2, H_2, N and H [7,8], but the fundamental aspects of the initial adsorption registries, adsorption energies, and structural parameters of hydrazine

* Corresponding author at: School of Chemistry, Cardiff University, Main Building, Park PI, Cardiff CF10 3AT, United Kingdom.
E-mail address: DzadeNY@cardiff.ac.uk (N.Y. Dzade).

https://doi.org/10.1016/j.apsusc.2019.02.128
Received 22 August 2018; Received in revised form 25 January 2019; Accepted 14 February 2019
Available online 18 February 2019
0169-4332/

on Ni surfaces remain unclear. Such information cannot be obtained directly from experiment and the underlying physical driving forces that control the reactivity of hydrazine with the Ni surfaces are therefore still not fully understood. However, electronic structure calculations based on the density functional theory (DFT) [9] provide an alternative way to gain fundamental insight into these processes, as they are capable of accurately predicting lowest-energy adsorption geometries and identifying charge transfer and other electronic effects [10–12].

Previous DFT calculations of hydrazine adsorption on nickel have focused on the perfect (111) [13,14] and (100) [9] surfaces, although real surfaces are never perfect and chemical processes often occur at defect sites. At the perfect (111) and (100) Ni surfaces, the hydrazine molecule was found to adsorb on the surface through one of its nitrogen atoms in its anti-conformation. When hydrazine is co-adsorbed with OH on the (111) surface, the cis-conformer was shown to be more stable due to electrostatic interactions between the OH and N_2H_4 [14]. In the present study, we have carried out a comprehensive study using dispersion-corrected DFT-D2 calculations to unravel the hydrazine adsorption conformations and properties, not only at the perfect (100), (110) and (111) nickel surfaces, but also at defective surfaces containing vacancies and Ni adatoms. The fundamental aspects of the adsorption process, including the hydrazine adsorption conformations, adsorption energies, and structural parameters are presented. Insight into the nature of the binding of hydrazine to the different surfaces was determined via analysis of projected density of states and differential charge density iso-surfaces.

2. Computational details

The electronic structure calculations were carried out within the plane-wave self-consistent field (PWscf) [10] code in Quantum ESPRESSO [16]. All calculations were spin-polarized and we have used the generalized gradient approximation (GGA) with the revised Perdew-Burke Ernzerhof (revPBE) [17–19] exchange-correlation functional to calculate the total free energies. The core electrons, up to and including the 3p levels of Ni and the 1s of O, were frozen and their interaction with the valence electrons was described by the projector augmented wave (PAW) method [18,19]. The Fermi surface effects were treated by the smearing technique of Gaussian, with a smearing parameter of 0.01 Ry. An energy threshold defining self-consistency of the electron density was set to 10^{-6} eV and a beta defining mixing factor for self-consistency of 0.2. A kinetic-energy cut-off of 35 Ry and charge density cut-off of 350 Ry were used for the smooth part of the electronic wave functions and the augmented electron density, respectively. Brillouin zone integration was achieved with $7 \times 7 \times 7$ and $3 \times 3 \times 1$ Monkhorst-Pack [20] k-point grids (centered at the Γ point) for bulk and surface slab models, respectively. Structural relaxation was carried out to minimize the energy using the conjugate gradient method of the Broyden–Fletcher–Goldfarb–Shanno (BFGS) algorithm [20,21], until the magnitude of the residual Hellmann–Feynman force on each relaxed atom reached 0.01 eV $Å^{-1}$. Long-range dispersion forces were accounted for in our calculations using the Grimme DFT-D2 method [22], with modification based on sound physical principles to the atom pairwise semi-empirical dispersion correction, as reported by Andersson [23], which is demonstrated to provide an accurate description of metallic systems. In the modified DFT-D2 scheme, a hard cut-off of 12 Bohr for the London dispersion was introduced to simulate the screening of the valence electrons, and the C_6 coefficient and dispersion radii for any transition metal are replaced with that of noble gases in the row above the relevant metal in the periodic table.

From a full geometry optimization, the equilibrium lattice parameter for Ni was predicted at 3.515 Å, which compares well with the experimental value of 3.522 Å [24] and an earlier reported theoretical value of 3.522 Å [25]. The computed cohesive and bulk moduli of 4.67 eV and 190.0 GPa also agree well with experimental values of 4.45 eV and 181.3 GPa, respectively. The different Ni surfaces were modelled using a periodic slab model, with the surfaces created using the METADISE code [26], which generates different atomic layer stackings resulting in a zero dipole moment perpendicular to the surface plane, as is required for reliable and realistic surface calculations. The slabs were constructed with six (6) atomic layers and a vacuum spacing of 20 Å was introduced in the z-direction to avoid interactions between periodic slabs. The relative stabilities of the nickel metal surfaces were determined according to their relaxed surface energy (γ_r), calculated as:

$$\gamma_r = \frac{E_{slab}^{relaxed} - nE_{bulk}}{2A} \quad (1)$$

where $E_{slab}^{relaxed}$ is the energy of the relaxed slab, nE_{bulk} is the energy of an equal number (n) of bulk Ni atoms, A is the area of the slab surface and the factor of 2 reflects the fact that there are two surfaces for each slab, which have identical atomic ordering at the bottom and top layers [19,27].

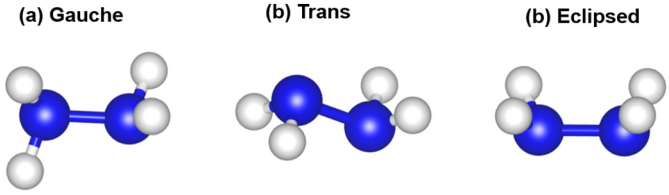

Fig. 1. Representation of the N_2H_4 conformations, (a) gauche, (b) trans, and (c) eclipsed.

The three major conformations of N_2H_4 in the gas phase, *gauche, trans* and *eclipse* (Fig. 1), were optimized prior to adsorption in a cubic box of size 10 Å. The *gauche* conformation of the molecule was predicted to be the most stable, followed by the *trans* and *eclipse* conformations, which, respectively, were 0.12 eV and 0.34 eV higher in energy, as shown in Table 1. The *gauche* and *trans* conformations were therefore chosen as hydrazine starting conformations for the combinatorial and systematic investigation of the adsorption of the molecule at the perfect nickel (100), (110) and (111) surfaces, as well as the defective surfaces containing vacancies and Ni adatoms. The hydrazine adsorption calculations were carried out on surface slabs constructed from (2×2) unit cells of the (100), (110) and (111) surfaces. These simulation supercells are large enough to minimize the lateral interactions between the hydrazine molecules in neighbouring image cells. Structural optimizations of the Ni–hydrazine systems were carried out without any symmetry constraint and, in particular, the hydrazine molecule was free to move away laterally and vertically from the initial binding site or reorient itself to find the minimum energy adsorption structure. All atoms of the hydrazine molecule and the topmost five atomic layers of the surface slabs were allowed to relax unconstrainedly until residual forces on all atoms reached 0.01 eV $Å^{-1}$. The bottom three layers were kept fixed at their equilibrium bulk value. To characterize the strength of N_2H_4 adsorption and to determine whether or not successful adsorption had occurred on each surface, we have calculated the energies of adsorption (E_{ads}) as follows:

$$E_{ads} = E_{slab+N_2H_4} - (E_{slab} + E_{mol}) \quad (2)$$

Table 1
Energetics and characteristics of hydrazine in three different conformations in the gas phase.

Conformation	Relative energy/eV	N–N (Å)	N–H (Å)	Dihedral θ, /°	NHN ϕ	NNH ϕ
Gauche	0.00	1.448	1.026	88.9	107.1	111.7
Trans	+0.118	1.498	1.026	171.1/82.3	102.5	103.3
Eclipsed	+0.336	1.498	1.026	2.0	103.8	109.6

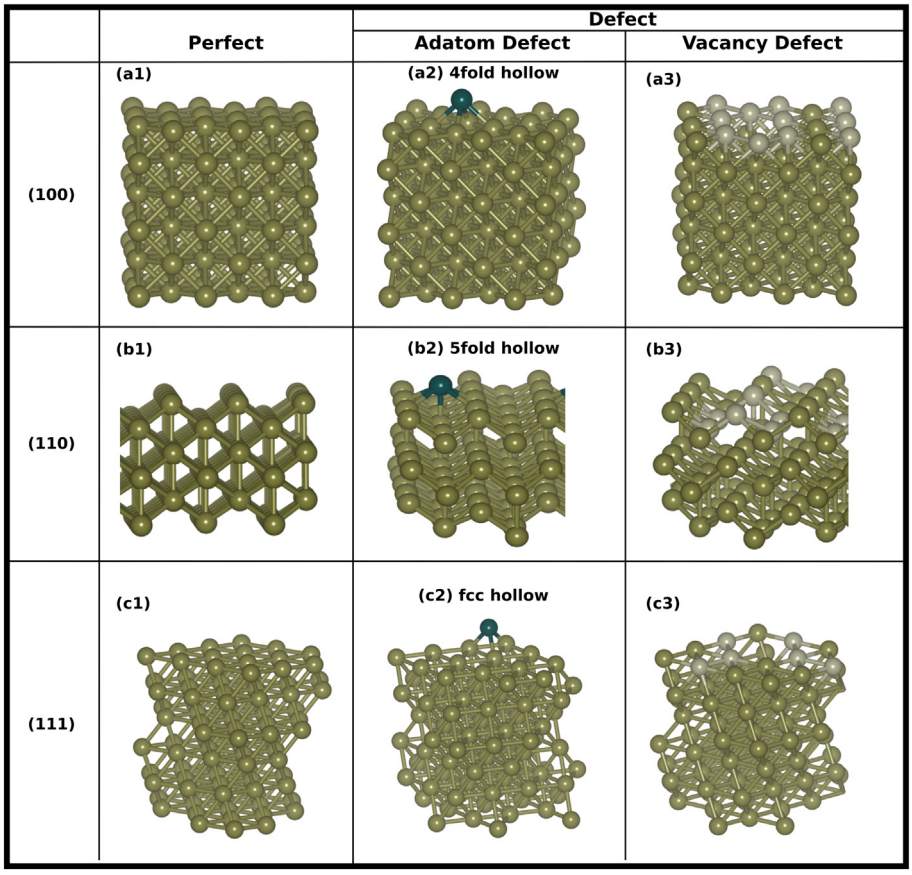

Fig. 2. Side view of the structures of the perfect and defect (adatom and vacancy) surfaces of Ni (100), (110) and (111). Ni atoms shown as gold, Ni adatom shown in teal, and Ni atoms around Ni vacancy shown in paler gold.

According to the above definition, a negative value indicates an exothermic and favourable adsorption process, whereas a positive value corresponds to an unfavourable endothermic process.

3. Results and discussions

3.1. Surface properties

The perfect low Miller index Ni (100), (110) and (111) surfaces, as shown in Fig. 2, were created from the fully optimized bulk face-centred cubic (FCC) Ni metal in order to eliminate the presence of spurious forces during surface relaxation. The (111) surface was predicted to be the thermodynamically most stable facet with a relaxed surface energy of 1.56 Jm^{-2}, in agreement with earlier theoretical predictions of Zhang et al. [28], Mittendorfer et al. [29], Vitos et al. [30] and Hong et al. [31], who reported values of 1.95, 1.93, 2.01 and 2.02 Jm^{-2}, respectively. The (100) and (110) surfaces have predicted surface energies of 2.41 and 2.42 Jm^{-2}, respectively, both of which are also in close agreement with earlier theoretical predictions. Mittendorfer et al.'s calculations [29] using PW91 [17] gave values for the Ni (100) and (110) surfaces of 2.19 and 2.25 Jm^{-2}, respectively, while a full charge density LMTO calculation by Vitos et al. [30] obtained 2.43 and 2.37 Jm^{-2}, respectively. Despite small differences in our calculated surface energies compared to those of earlier theoretical investigations, the predicted stability order of $\gamma(111) < \gamma(100) < \gamma(110)$ is consistent with Zhang et al.'s [28], Mittendorfer et al.'s [29] and Hong et al.'s [31] GGA calculations.

Considering that experimental surfaces are not generally perfect, we have also created two kinds of defects (adatoms and vacancies) on each surface. Adatom point defects were investigated by adding one Ni atom on one side of each slab at various surface sites, including top, bridge, 4-fold and 3-fold sites, whereas vacancy defects were created by removing one Ni atom from one side of each slab at various surface sites (see Fig. 2). To determine which point defect is energetically more favourable and most likely to be formed at the Ni surfaces, we have calculated the adatom and vacancy formation energies as reported in Table 2. It can be seen from the calculated formation energies that the preferred adsorption location for the added Ni atoms on the (100) and (110) surfaces is at the 4-fold hollow site, whereas on the (111) surface it is at the 3-fold hollow site. The Ni adatom formation energies at the (100), (110) and (111) surfaces were calculated at 0.71, 0.52 and 0.73 eV, respectively. Vacancy defect formation is found to be favoured most on the Ni(110) surface with an energy of 0.39 eV, compared to the Ni(100) and Ni(111) surfaces, which have vacancy formation energies

Table 2
Defect formation (E_f) and surface (γ) energies of perfect Ni (100), (110) and (111) surfaces.

Surface (site)	Formation energy, E_f, eV			Surface energy, γ (Jm^{-2})		
	(100)	(110)	(111)	(100)	(110)	(111)
Perfect	–	–	–	2.41	2.42	1.56
Adatom atop	1.91	2.59	1.38	3.03	3.02	2.64
Adatom bridge	1.37	1.82 (s-bridge) 0.81 (l-bridge)	0.85	2.85	2.84 (s-bridge) 2.61 (l-bridge)	2.46
Adatom hollow	0.71	0.52	0.73 (fcc) 0.73 (hcp)	2.64	2.54	2.42 (fcc) 2.42 (hcp)
Vacancy	0.57	0.39	0.70	2.59	2.51	2.41

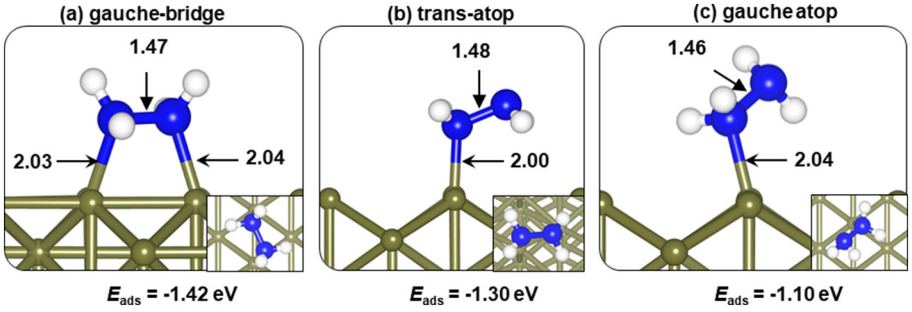

Fig. 3. Lowest-energy N_2H_4 adsorption configurations on perfect Ni(110) surface (Ni = gold, N = blue, H = white).

of 0.57 and 0.70 eV, respectively.

Considering the surface structures with the lowest adatom formation energies, the surface energies of the (100), (110) and (111) adatom surfaces were calculated at 2.64, 2.54 and 2.42 Jm^{-2}, respectively. The surface energies of the (100), (110) and (111) surfaces containing vacancy defects were calculated at 2.59, 2.51 and 2.41 Jm^{-2}, respectively. It is worth noting that the surface energies of the defective surfaces are higher than those of the perfect surfaces, which suggests that the creation of adatoms and vacancy point defects on the (100), (110) and (111) Ni surfaces have a destabilizing effect on the surfaces, due the presence of a low-coordinated sites. However, the surface energies of the defective and perfect surfaces are close enough that we may expect these surface defects to occur under experimental conditions.

3.2. Adsorption of N_2H_4 on the perfect and defective Ni (110) surfaces

A number of adsorbed hydrazine configurations were explored at high symmetry sites on the perfect Ni (110) surface in order to determine the lowest-energy adsorption structures. Shown in Fig. 3 are the three lowest-energy adsorption configurations obtained on the perfect Ni(110) with the structural and energetic details listed in Table 3. The preferred adsorption configuration is calculated to be the *gauche*-bridge complex (Fig. 3a) in which N_2H_4 binds through both nitrogen atoms to the surface with Ni–N distances of 2.039 Å and 2.042 Å. The adsorption energy of this structure is calculated at −1.43 eV, with the N–N bond distance and dihedral angle calculated at 1.466 Å and 69.8°, respectively, as shown in Table 3. The *gauche*-bridge configuration is found to be 0.12 eV and 0.32 eV more stable, respectively, than the trans-atop (Fig. 3b) and gauche-atop (Fig. 3c) configurations, where the N_2H_4 binds through only one nitrogen atom to the surface with Ni–N distances of 2.039 Å and 2.042 Å, respectively. The N–N bond distance and the dihedral angle were calculated at 1.480 Å and 177.5° for the trans-atop configuration and 1.462 Å and 101.4° for the *gauche*-atop configuration.

On the Ni/Ni(110) surface, with a Ni adatom located at the preferred 4-fold hollow site, we have investigated the adsorption of N_2H_4 near the adatom site in a number of different starting configurations, as on the perfect Ni(110) surface. Displayed in Fig. 3 are the lowest-energy N_2H_4 adsorption structures at the Ni/Ni(110) surface. The most stable adsorption is calculated for the *gauche*-bridge-surf structure (Fig. 4a), which released an adsorption energy of 1.40 eV/N_2H_4. In the lowest-energy *gauche*-bridge-surf structure, N_2H_4 binds through both nitrogen atoms to surface Ni sites at Ni–N distances of 2.046 Å and 2.040 Å. The N–N bond distance and torsion angle were calculated to be 1.463 Å and 62.2°, respectively. The adsorption energies of the other stable nickel-hydrazine structures are calculated at −1.34 eV for the trans-atop-adatom, −1.27 eV for the *gauche*-bridge-adatom, −1.31 eV for the *gauche*-atop-adatom, and −1.00 eV for the gauche-atop-surf configurations, respectively, as shown in Fig. 4 and Table 3.

The vacancy defect on the Ni(110) surface allows for three low-energy nickel-hydrazine adsorption configurations, i.e. the gauche-bridge, trans-atop and gauche-bridge, as shown in Fig. 5. The gauche-bridge and the trans-atop configurations result in very similar adsorption energies calculated at −1.43 eV and –1.42 eV, differing by only 0.01 eV. The gauche-bridge configuration is predicted to be 0.11 eV more stable than the gauche-atop configuration, which binds via only one nitrogen atom to a surface Ni near the vacancy site. The lowest-energy gauche-bridge N_2H_4 adsorption structure predicted at the (110) surface with vacancy sites is almost equivalent to the one obtained at the perfect (110) surface and the adsorption energies are nearly the same. Based on the calculated adsorption energies, it can be concluded that N_2H_4 will preferentially adsorb in a bridging mode at the Ni(110) surface irrespective of the nature of the surface, perfect or defective.

3.3. Adsorption of N_2H_4 on the perfect and defective Ni(100) surfaces

As with the Ni(110) surface, we have explored different starting configurations of N_2H_4 at high symmetry sites on the Ni(100) surface in order to determine lowest-energy adsorption configurations, as shown in Fig. 6. The most stable N_2H_4 adsorption configuration on the perfect Ni(100) surface is calculated to be *gauche*-bridge configuration (Fig. 6a) with an adsorption energy of −1.27 eV (Table 4). In this configuration, the N_2H_4 molecule adsorbs on the surface in a bridging mode through

Table 3
Adsorption energies and geometries of N_2H_4 adsorbed on perfect, ad-atom and vacancy defect Ni (110) surface.

Surface	Configuration	E_{ad}/eV	E_{ads}^{vDW}	N–N/(Å)	N1–Ni/(Å)	N2–Ni/(Å)	Ni-H_{AVG}/(Å)	Dihedral, θ/°	Inclination Ang/°
Perfect	*Gauche*-bridge	−1.43	−0.49	1.466	2.039	2.042	1.030	69.8	102.8/102.0
	Trans-atop	−1.29	−0.47	1.480	2.019	–	1.031	177.5/71.9	115.1
	Gauche-atop	−1.10	−0.43	1.462	–	2.019	1.030	101.4	116.3
Adatom	Gauche-bridge-Surf	−1.39	−0.54	1.463	2.046	2.040	1.031	62.2	101.7/101.4
	Trans-atop-adatom	−1.34	−0.23	1.492	–	1.960	1.028	176.9/70.1	116.2
	Eclipse-ridge-adatom	−1.28	−0.45	1.506	2.019	2.020	1.029	12.7	106.7/101.6
	Gauche-atop-adatom	−1.21	−0.28	1.473	–	1.984	1.027	109.9	114.2
	Gauche-atop-surf	−0.98	−0.52	1.456	–	2.034	1.028	91.0	121.5
Vacancy	Gauche-bridge	−1.43	−0.466	1.469	2.045	2.032	1.031	59.6	102.7/102.60
	Trans-atop	−1.42	−0.459	1.480	–	2.007	1.030	165.0/88.5	117.7
	Gauche-atop	−1.34	−0.42	1.459	–	2.037	1.032	84.2	116.6

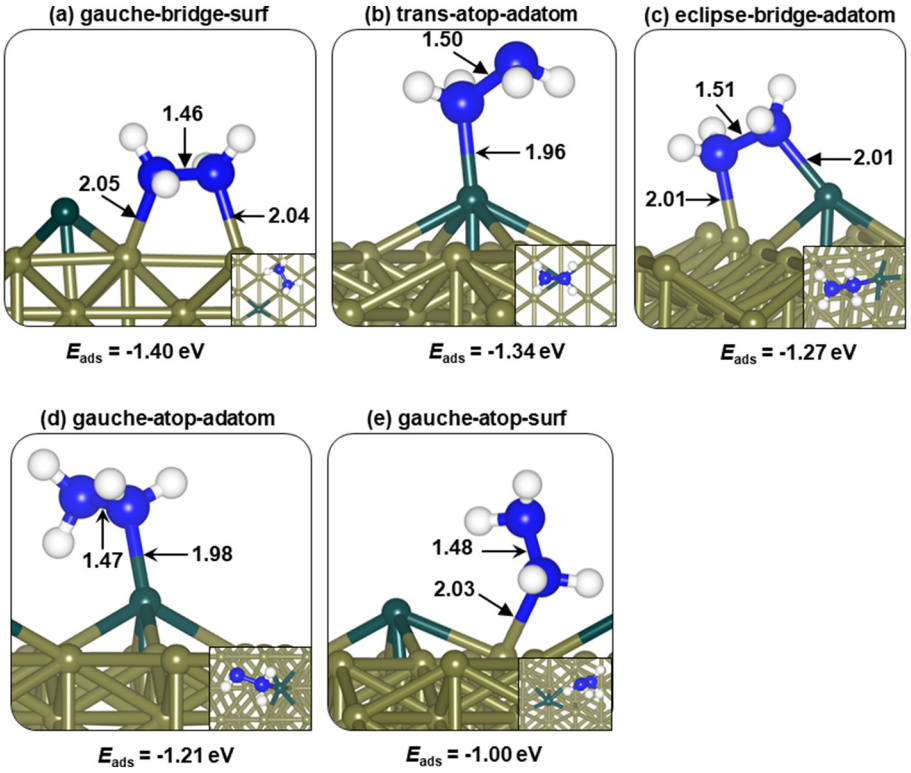

Fig. 4. Lowest-energy N_2H_4 adsorption configurations on ad-atom Ni/Ni(110) surface (Ni = gold, Ni adatom = teal, N = blue, H = white).

both nitrogen atoms, interacting with surface Ni atoms at an average Ni—N distance of 2.037 Å. The N—N bond length and the dihedral angle were calculated at 1.467 Å and 104.2°, respectively. The *trans-atop* N_2H_4 configuration released an adsorption energy of 1.24 eV, which is 0.03 eV less favourable than the most stable gauche-bridge configuration. In the trans-atop configuration, the hydrazine molecule adsorbs through one nitrogen atom at a Ni—N bond distance of 1.995 Å and the N—N bond distance and the dihedral angle were calculated at 1.476 Å and 178.1°, respectively. Compared to the most stable *gauche*-bridge configuration calculated in the present work, Agusta et al. predicted an anti-conformation [13–15]. The difference in the two results can be attributed to the absence in the work by Agusta et al. to account for dispersion forces, which inclusion has only been fairly recently added to DFT capabilities. However, dispersion forces contribute to the overall binding energy and thus play an important role in the accurate prediction of the lowest-energy adsorption configurations of molecules on surfaces and.

On the Ni(100) surface with the Ni adatom preferentially located at the 4-fold hollow site, five low-energy N_2H_4 adsorption configurations were identified namely the trans-atop-surf, trans-atop-adatom, *gauche*-bridge-adatom, gauche-atop-adatom and gauche-bridge-surf, as shown in Fig. 7. Among these configurations, the trans-atop-surf (Fig. 7a) is calculated as the thermodynamically most stable configuration with an adsorption energy of −1.30 eV. In this configuration, the N_2H_4 binds onto the surface through one N—Ni bond (2.000 Å) with the N—N bond calculated at 1.472 Å (Table 4). The other stable configurations released similar adsorption energies, calculated at 1.17 eV for trans-atop-adatom, 1.14 eV for *gauche*-bridge-adatom, 1.01 eV for gauche-atop-adatom, and 1.00 eV for the gauche-bridge-surf configuration (Fig. 7). In the trans-atop-adatom and gauche-atop-adatom configurations, the N_2H_4 molecule binds at the Ni adatom site via one N—Ni bond calculated at 1.960 Å and 2.000 Å, respectively. In the *gauche*-bridge-adatom configuration (Fig. 7c), one of the N atoms interacts with the Ni adatom ($N–Ni_{adatom}$ = 2.053 Å), whereas the other N atom interacts with a surface Ni site ($N–Ni_{surf}$ = 2.055 Å). In the *gauche*-bridge-surf configuration the N_2H_4 adsorbs near the Ni adatom with both N atoms interacting with the surface Ni sites (N–Ni = 2.129, 2.009 Å).

The adsorption of N_2H_4 on the Ni(100) surface with a Ni vacancy defect results in three low-energy hydrazine-nickel configurations, i.e. gauche-bridge-near-vac, trans-atop and gauche-bridge-surf, as shown in Fig. 8. The gauche-bridging configuration (Fig. 8a) was calculated as the preferred hydrazine-nickel configuration with an adsorption energy

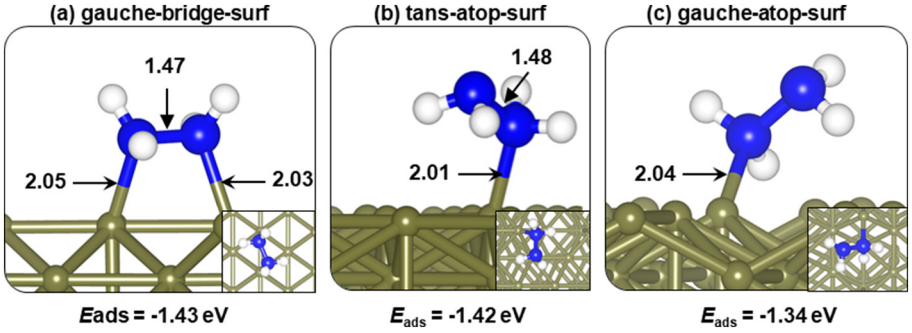

Fig. 5. Lowest-energy N_2H_4 adsorption configurations on vacancy defect Ni(110) surface (Ni = gold, N = blue, H = white).

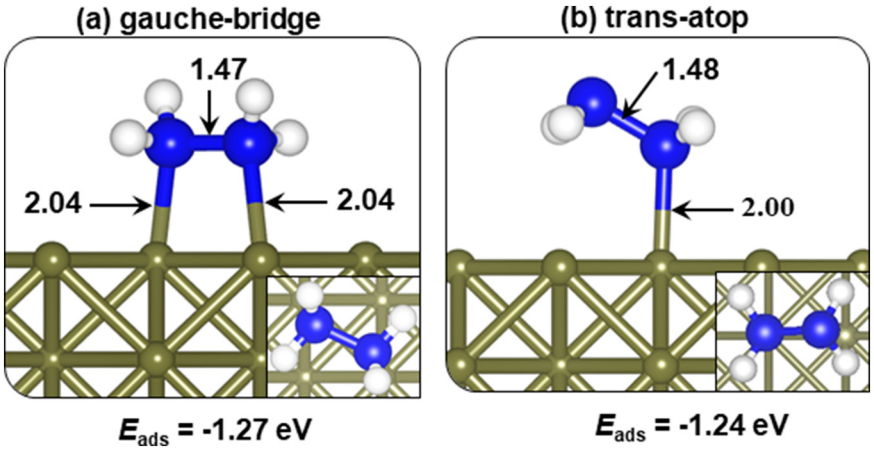

Fig. 6. Lowest-energy N_2H_4 adsorption configurations on perfect Ni(100) surface (Ni = gold, N = blue, H = white).

of −1.66 eV. Besides being the most stable configuration on the vacancy defect surface, it is also the thermodynamically preferred structure overall on the Ni(100) surface, considering both the perfect and defective surfaces. In the lowest-energy *gauche*-bridging configuration, the N_2H_4 molecule binds through both N atoms at Ni atoms near the vacancy site, at Ni—N bond distances of 2.168 Å and 2.088 Å. The N—N bond is calculated at 1.476 Å, whereas the dihedral and inclination angles were 70.5°. The trans-atop (Fig. 8b) and *gauche*-surf-bridge (Fig. 8c) configurations released adsorption energies of 1.34 and 1.17 eV, respectively. The structural parameters of the adsorbed N_2H_4 and interatomic bond distances are summarized in Table 4.

3.4. Adsorption of N_2H_4 on the perfect and defective Ni(111) surfaces

The perfect Ni(111) surface is the thermodynamically most stable surface among the low-Miller index facets of FCC nickel. Three stable adsorption configurations of N_2H_4 were calculated on the perfect Ni (111): trans-atop, eclipse-bridge and *gauche*-atop, as shown in Fig. 9. The trans-atop configuration (Fig. 9a) was the most stable configuration with an adsorption energy of −1.18 eV. The interacting Ni—N bond distance was calculated at 2.022 Å and the N—N bond converged at 1.475 Å, with the dihedral and inclination angles predicted to be 180.0° and 145.4°, respectively (Table 5). The eclipse-bridge and *gauche*-atop configurations released very similar adsorption energies of −1.10 eV and −1.09 eV, respectively. In the eclipse-bridge configuration, the N_2H_4 binds through both N atoms at N–Ni distances of 2.075 and 2.060 Å, whereas it binds via just one N atom in the *gauche*-atop configuration at a N–Ni distance of 2.049 Å.

At the Ni/Ni(111) surface with a Ni adatom adsorbed at the hcp or fcc site, six low-energy nickel-hydrazine configurations were determined, as shown in Fig. 10. The *gauche*-bridge-adatom configuration (Fig. 10a) was calculated to be the preferred adsorption configuration releasing an adsorption energy of 1.56 eV. In this configuration, the hydrazine molecule binds in a bridging mode with one of its nitrogen atoms interacting with the Ni adatom ($N–Ni_{adatom}$ = 2.035 Å) and the other with a surface Ni site ($N–Ni_{surf}$ = 2.075 Å). The calculated N—N bond is 1.475 Å, whereas the dihedral and inclination angles were calculated at 71.2° and 112.9°, respectively. The other stable adsorption configurations released adsorption energies of 1.44, 1.29, 1.27, 1.08, and 0.98 eV, respectively, for the *gauche*-atop-surf, gauche-atop-adatom, trans-atop-adatom, trans-atop-surf and eclipse-bridge-surf configurations, as shown in Fig. 10 and Table 5. On the Ni(111) surface with one Ni vacancy site, three low-energy nickel-hydrazine structures were found, i.e. the gauche-bridge, trans-atop and the gauche-atop configurations (Fig. 11), which released adsorption energies of 1.06, 0.89, and 0.82 eV, respectively. In the most stable gauche-bridge configuration, the N_2H_4 molecule binds through both N atoms to Ni atoms near the vacancy site with the Ni—N bond distances calculated at 2.066 Å and 2.028 Å. The N—N bond distance converged at 1.466 Å, whereas the dihedral and inclination angles were obtained at 56.3° and 99.6°. In the trans-atop and the gauche-atop configurations, N_2H_4 binds to Ni atoms through only one N atom at Ni—N bond distances of 2.014 Å and 2.034 Å, respectively. The closest H-surface interatomic bond distances were calculated at 1.031 Å for both gauche-bridge and trans-atop configuration, and at 1.028 Å for the gauche-atop configuration.

3.5. Electronic structure

To gain insight into the nature of the interaction and electronic structure of the systems of adsorbed hydrazine on the Low-Miller index Ni (100), (110) and (111) surfaces, the projected density of states (PDOS) and the differential charge density (Δρ) iso-surfaces of the most stable N_2H_4-surface configurations at the different surfaces were determined (Figs. 12 − 14). The PDOS plots reveal hybridization between the surface Ni *d*-states and the N *p*-orbitals, which is consistent with the observed chemisorptive character of N_2H_4 on the different Ni surfaces

Table 4
Adsorption energies and geometries of N_2H_4 on perfect, ad-atom and vacancy defect Ni (100).

Surface	Configuration	E_{ad}/eV	E_{ads}^{vDW}	N–N/(Å)	N1–Ni/(Å)	N2–Ni/(Å)	Ni-H_{AVG}/(Å)	dihedral/θ	Inclination Ang/°
Perfect	Gauche-bridge	−1.27	−0.57	1.467	2.036	2.038	1.031	104.2/104.6	104.6/105.1
	trans-atop	−1.24	−0.52	1.476	–	1.995	1.030	178.1/75.4	118.8
Adatom	Trans-atop-surf	−1.32	−0.60	1.472	–	2.000	1.032	179.6/73.5	119.0
	Trans-adatom-atop	−1.17	−0.57	1.490	–	1.960	1.029	176.9/75.9	112.4
	Gauche-bridge-adatom	−1.14	−0.46	1.470	2.055	2.053	1.031	58.7	104.5/97.3
	Gauche-atop-adatom	−1.02	−0.16	1.473	–	2.00	1.026	111.2	115.8
	Gauche-bridge-surf	−1.00	−0.64	1.461	2.129	2.009	1.032	49.8	102.7
Vacancy	Gauche-bridge-vac	−1.66	−0.73	1.476	2.168	2.088		70.5	108.9/118.5
	trans-atop	−1.34	−0.52	1.475	–	2.007	1.031	171.2/63.2	120.3
	Gauche-bridge-surf	−1.17	−0.48	1.470	2.041	2.037	1.030	48.4	106.5/104.3

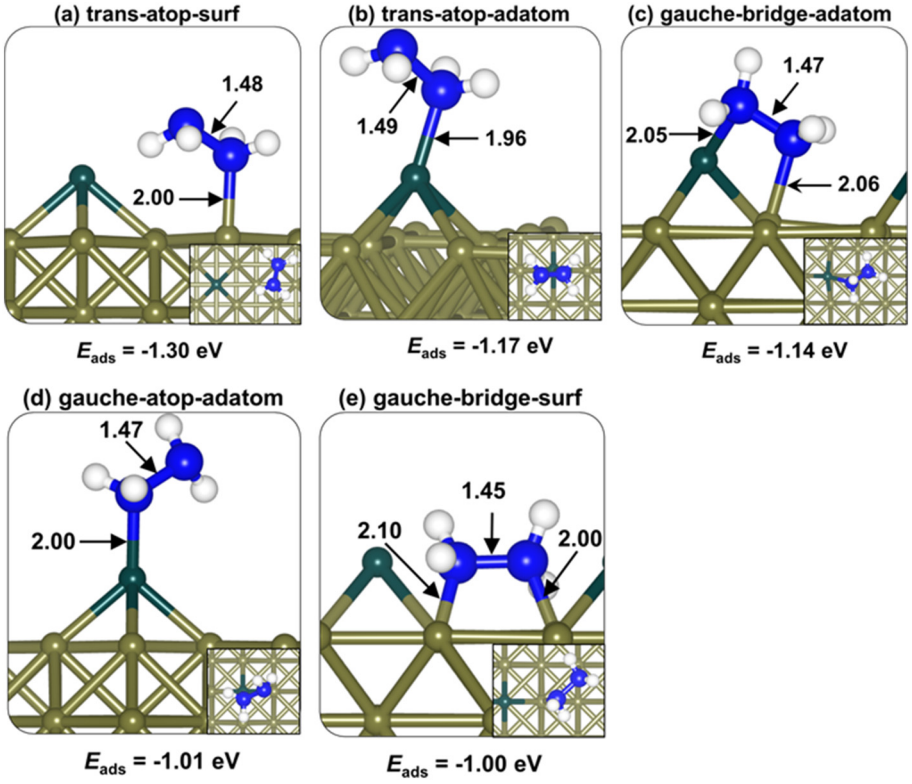

Fig. 7. Lowest-energy N_2H_4 adsorption configurations on ad-atom Ni/Ni(100) surface (Ni = gold, Ni adatom = teal, N = blue, H = white).

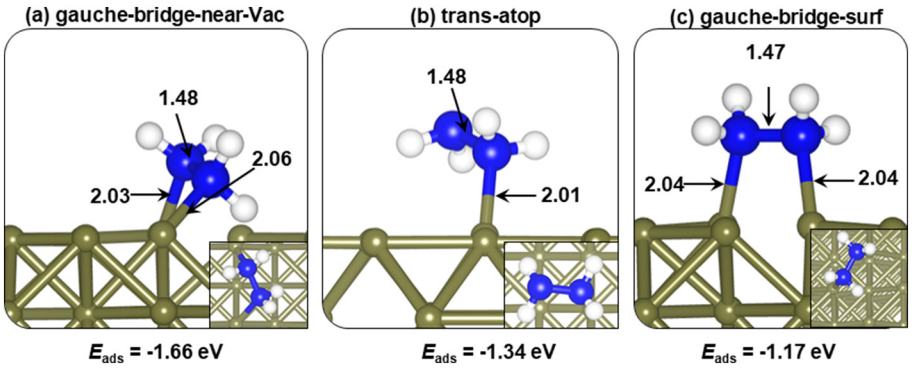

Fig. 8. Lowest-energy N_2H_4 adsorption configurations on vacancy defect Ni(100) surface (Ni = gold, N = blue, H = white).

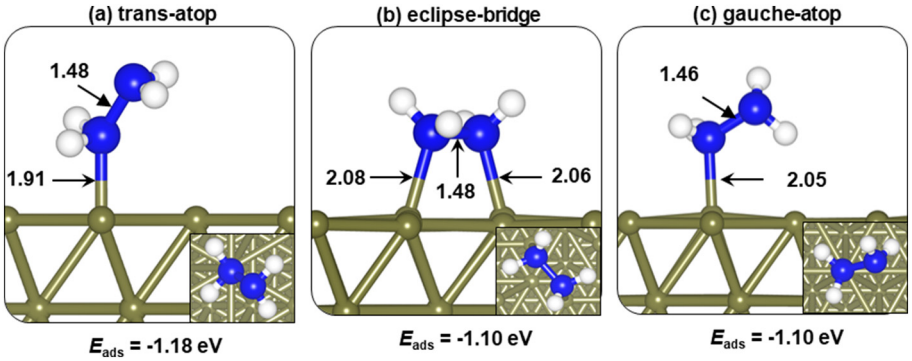

Fig. 9. Lowest-energy N_2H_4 adsorption configurations on perfect Ni(111) surface (Ni = gold, N = blue, H = white).

studied. We also found that depending on the binding mode of N_2H_4 on the Ni surface, i.e. either through a single or both nitrogen atoms, the N *p*-orbitals remain identical or become different upon adsorption. In Figs. 12a and 13a, the symmetry of the bridging configurations on the perfect (110) and (100) surfaces are shown by the identical electronic structure of the N *p*-orbitals. However, in the configurations in which only one of the N atoms interacts with the surface, we observe a shift to lower energies or a decrease in the DOS intensity for the nitrogen atom

Table 5
Adsorption energies and geometries of N_2H_4 on perfect, ad-atom and vacancy defect Ni (111) surface.

Surface	Configuration	E_{ad}/eV	E_{ads}^{vDW}	N–N/ (Å)	N1–Ni/ (Å)	N2–Ni/ (Å)	Ni-H_{AVG}/ (Å)	dihedral/θ	Inclination Ang/°
Perfect	Trans-atop	−1.18	−0.579	1.475	–	2.022	1.030	180.0/68.9	145.4
	Eclipse-bridge	−1.10	−0.590	1.476	2.060	2.075	1.029	35.2	103.6/104.5
	Gauche-atop	−1.09	−0.520	1.460	–	2.049	1.027	100.6	118.3
Adatom	Gauche-bridge-adatom	−1.56	−0.58	1.475	2.035	2.075	1.031	71.2	112.9/108.3
	Gauche-atop-surf	−1.44	−0.53	1.448	–	2.052	1.024	76.5	115.6
	Gauche-atop-adatom	−1.29	−0.17	1.471	–	2.009	1.027	104.4	115.1
	Trans-atop-adatom	−1.27	−0.17	1.493	–	1.973	1.028	172.8/79.1	120.6
	Trans-surf-atop	−1.08	−0.62	1.474	–	2.019	1.032	179.1/74.2	117.7
	Eclipse-surf-bridge	−0.98	−0.67	1.482	2.042	2.034	1.032	17.9	104.6/104.5
Vacancy	Gauche-bridge	−1.06	−0.529	1.466	2.066	2.028	1.031	56.3	99.6/104.0
	Trans-atop	−0.89	−0.560	1.476	–	2.014	1.031	175.1/78.1	118.5
	Gauche-atop	−0.82	−0.546	1.463	–	2.034	1.028	106.5	116.6

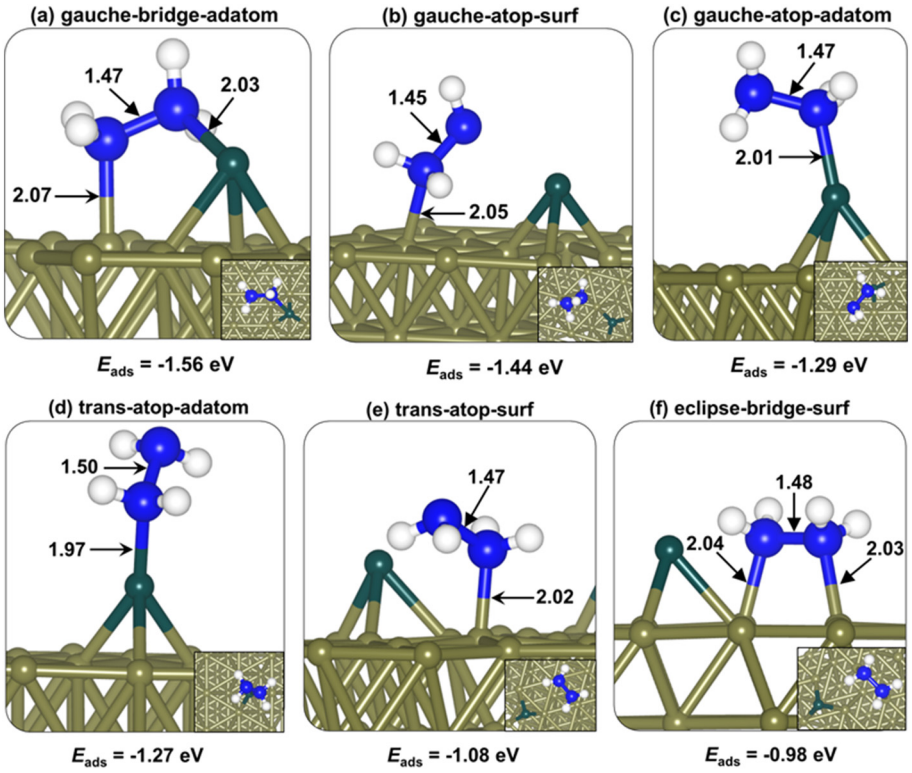

Fig. 10. Lowest-energy N_2H_4 adsorption configurations on ad-atom Ni/Ni(111) surface (Ni = gold, Ni adatom = teal, N = blue, H = white).

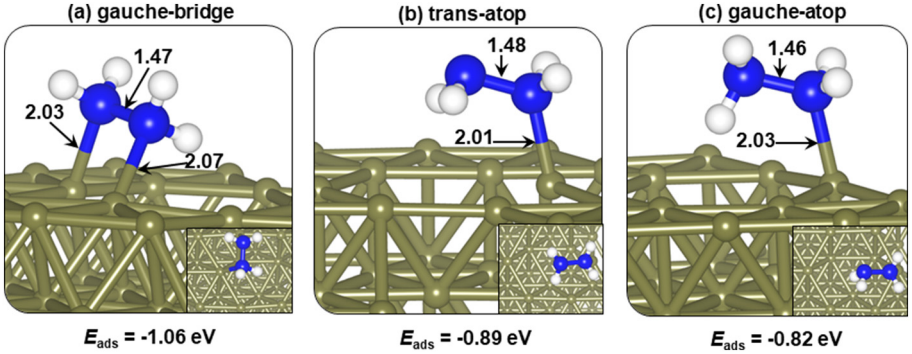

Fig. 11. Lowest-energy N_2H_4 adsorption configurations on vacancy defect Ni(111) surface (Ni = gold, N = blue, H = white).

closer to the surface.

The differential charge densities were obtained by subtracting from the charge density of the total N_2H_4-surface systems the sum of the charge densities of the adsorbate N_2H_4 molecule and the Ni surface, with the atomic positions of the Ni surface and of the N_2H_4 molecule kept the same as those of the total N_2H_4-surface systems. In this way, the presentation highlights the local electron density rearrangement and bond formation in the N_2H_4-surface systems. An analysis of the

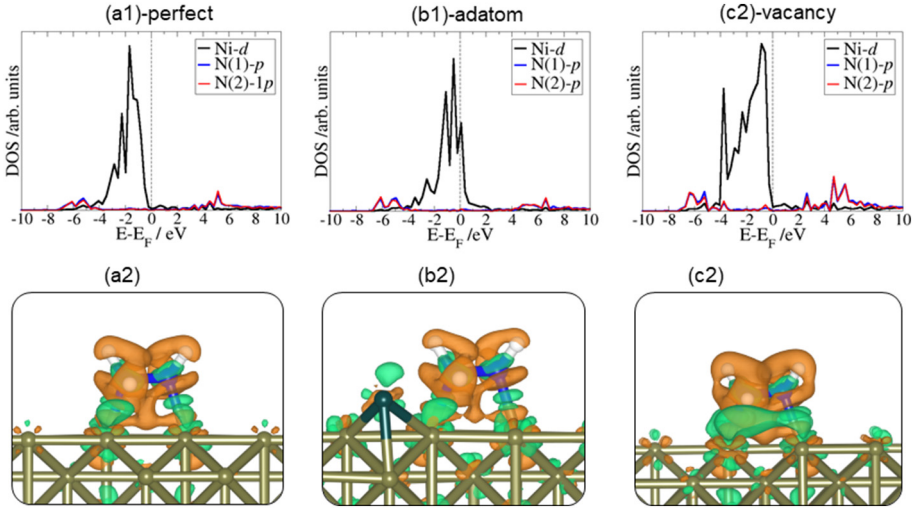

Fig. 12. Projected density of states (top) and corresponding iso-surface of differential charge density (below) of most stable N_2H_4 adsorption configurations on Ni (110) surfaces: perfect, with adatom and with Ni vacancy.

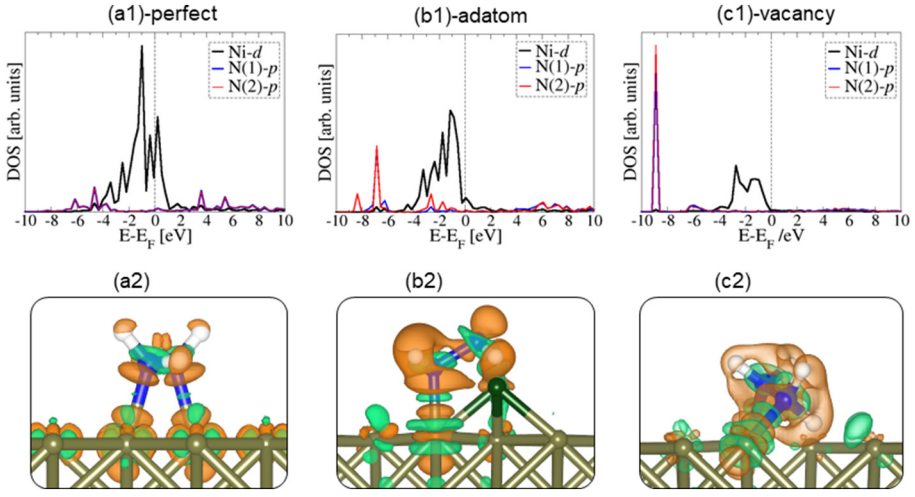

Fig. 13. Projected density of states (top) and corresponding iso-surface of differential charge density (below) of most stable N_2H_4 adsorption configurations on Ni (100) surfaces: perfect, with adatom and with Ni vacancy.

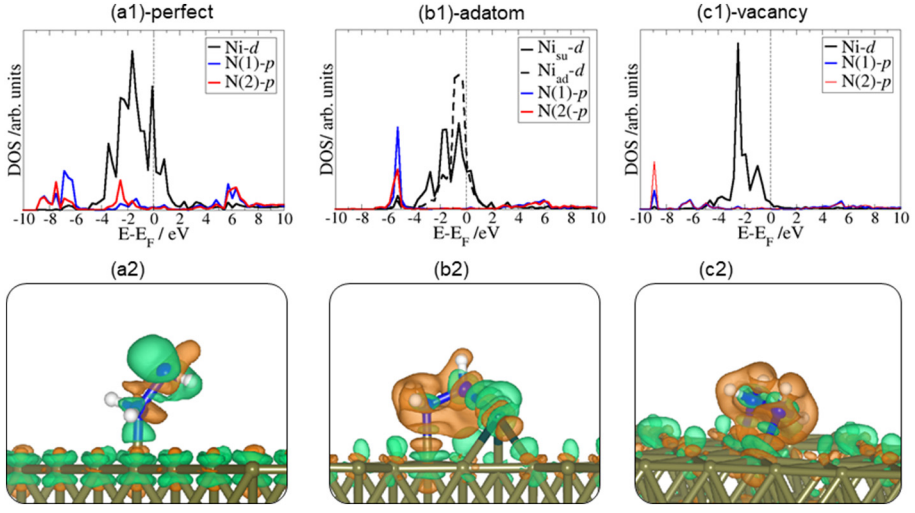

Fig. 14. Projected density of states (top) and corresponding iso-surface of deferential charge density (below) of most stable N_2H_4 adsorption configurations on Ni (111) surfaces: perfect, with adatom and with Ni vacancy.

Table 6
Bader population analysis of adsorbed hydrazine on the different Ni surfaces. The atomic charges of gas-phase hydrazine are also reported.

Surface	State	N1	N2	H1	H2	H3	H4	Total
	Gas-phase	−0.81	−0.78	0.42	0.41	0.37	0.39	0.00
Ni(110)	Perfect	−0.88	−0.85	0.46	0.50	0.43	0.43	0.09
	Adatom	−0.88	−0.82	0.47	0.40	0.47	0.45	0.09
	Vacancy	−0.86	−0.80	0.46	0.42	0.42	0.42	0.06
Ni(100)	Perfect	−0.82	−0.85	0.43	0.43	0.43	0.46	0.08
	Adatom	−0.85	−0.84	0.48	0.43	0.43	0.42	0.07
	Vacancy	−0.84	−0.83	0.45	0.42	0.40	0.45	0.05
Ni(111)	Perfect	−0.86	−0.75	0.43	0.46	0.39	0.41	0.08
	Adatom	−0.85	−0.81	0.47	0.42	0.37	0.45	0.05
	Vacancy	−0.85	−0.86	0.46	0.43	0.43	0.47	0.08

differential charge density isosurface contours (inserts in Figs. 12−14) reveal electron density accumulation within the N–Ni bonding regions, which is consistent with observed hybridization between the surface Ni *d*-states and the N *p*-orbitals. We also see electron density accumulation between the hydrogen and surface Ni atoms, indicative of hydrogen-bonded interactions, which contribute to the stabilization of the N_2H_4 molecules. Charge transfer between the surface and the adsorbing hydrazine was characterized using the space partitioning scheme of the Bader analysis (Table 6). From the calculated Bader charges, it is evident that N atoms gain charge from the interacting Ni ions resulting in their increased negative charges. However, the increase in the positive charges of the H atoms suggests that there is a back-donation of charges from the hydrogen atom to the surfaces. The resulting net positive charge calculated for the hydrazine molecule in all the Ni-hydrazine adsorption systems, suggests that the adsorption process is characterized overall by a net charge transfer from the hydrazine to the Ni surfaces. However, we have not identified any trend between the amount of charge transferred and the calculated adsorption energies of N_2H_4 at the different Ni surfaces, suggesting that the variation in strength of N_2H_4 binding may be an effect of the coordination of the interacting surface Ni atoms, which also dictates the N−Ni bond distances.

4. Conclusion

We have employed first-principles DFT-based calculations with long-range interaction corrections in a systematic study of the adsorption of N_2H_4 on the perfect Ni (110), (100), and (111) surfaces, as well as the same surfaces containing two types of point defects, i.e. Ni adatoms and vacancies). The hydrazine molecule is shown to interact with the Ni surfaces mainly through the lone-pair of electrons located on the N atoms, forming either monodentate or bidentate bonds with the surface. The strength of N_2H_4 adsorption on the perfect surfaces is found to be related to their stability with the energy released upon adsorption decreasing in the order (110) > (100) > (111). Hydrazine adsorbs most strongly onto the least stable (110) surface via both N atoms in a *gauche*-bridge configurations and most weakly onto the most stable (111) surface via one N–Ni bond. The creation of defects in the form of Ni adatoms and vacancies provides lower-coordinated Ni sites, allowing stronger hydrazine adsorption. The preferred adsorption configuration of N_2H_4 on any of the perfect and defective surfaces is obtained when the hydrazine molecule bridges two surface Ni atoms through both N atoms, except on the perfect (110) and adatom (100) surfaces, where a structure with only one N on a top site is preferred, with the hydrazine in trans-atop conformations. Analysis into the bonding nature of N_2H_4 onto the Ni surfaces reveals that the adsorption is characterized by strong hybridization between the surface Ni *d*-states and the N *p*-orbitals, which is corroborated by electron density accumulation within the newly formed N–Ni bonding regions.

Acknowledgments

We acknowledge the Royal Society and the Leverhulme Trust, UK for funding, as well as support by the National Council for Tertiary Education (NCTE), Ghana, through the Teaching and Learning Innovation Fund (TALIF-NUSTR/3/008/2005).

References

[1] K. Yamada, K. Asazawa, K. Yasuda, T. Ioroi, H. Tanaka, Y. Miyazaki, T. Kobayashi, Investigation of PEM type direct hydrazine fuel cell, J. Power Sources 115 (2003) 236–242.
[2] M.R. Andrew, W.J. Gressler, J.K. Johnson, R.T. Short, K.R. Williams, Engineering aspects of hydrazine-air fuel-cell power systems, J. Appl. Electrochem. 2 (1972) 327–336.
[3] K. Asazawa, T. Sakamoto, S. Yamaguchi, K. Yamada, H. Fujikawa, H. Tanaka, K. Oguro, Study of anode catalysts and fuel concentration on direct hydrazine alkaline anion-exchange membrane fuel cells, J. Electrochem. Soc. 156 (2009) B509–B512.
[4] K. Asazawa, K. Yamada, H. Tanaka, A. Oka, M. Taniguchi, T. Kobayashi, A platinum-free zero-carbon-emission easy fueling direct hydrazine fuel cell for vehicles, Angew. Chem. 119 (2007) 8170–8173.
[5] J. Sanabria-Chinchilla, K. Asazawa, T. Sakamoto, K. Yamada, H. Tanaka, P. Strasser, Noble metal-free hydrazine fuel cell catalysts: EPOC effect in competing chemical and electrochemical reaction pathways, J. Am. Chem. Soc. 133 (2011) 5425–5431.
[6] S. Arrhenius, Z. Phys. Chem. 4 (1889) 226 (translated into English in *Selected Readings in Chemical Kinetics*, edited by M.H. Back and K.J. Laidler (Oxford, NY) (1967)).
[7] K.J. Laidler, The development of the Arrhenius equation, J. Chem. Educ. 61 (1984) 494.
[8] N.Y. Dzade, A. Roldan, N.H. de Leeuw, Surface and shape modification of mackinawite (FeS) nanocrystals by cysteine adsorption: a first-principles DFT-D2 study, Phys. Chem. Chem. Phys. 18 (2016) 32007–32020.
[9] S.G. Pakdehi, M. Salimi, M. Rasoolzadeh, A review on decomposition of hydrazine and its kinetics as a novel approach for CO free H_2 production, Res. Appl. Mech. Eng. 3 (2014) 21–25.
[10] S. Baroni, A. Dal Corso, S. de Gironcoli, P. Giannozzi, PWSCF and PHONON: Plane-wave Pseudo-potential Codes, (2001).
[11] N.Y. Dzade, A. Roldan, N.H. de Leeuw, Adsorption of methylamine on mackinawite (FeS) surfaces: a density functional theory study, J. Chem. Phys. 139 (2013) 124708.
[12] N.Y. Dzade, A. Roldan, N.H. de Leeuw, Structures and properties of $As(OH)_3$ adsorption complexes on hydrated mackinawite (FeS) surfaces: a DFT-D2 study, Environ. Sci. Technol. 51 (2017) 3461–3470.
[13] M.K. Agusta, H. Kasai, First principles investigations of hydrazine adsorption conformations on Ni (111) surface, Surf. Sci. 606 (2012) 766–771.
[14] M.K. Agusta, P.H. Purwoko, A.G. Saputro, F. Fathurrahman, H.K. Dipojono, W.A. Diño, Conformational effects on hydrazine and OH coadsorption on Ni (111): a first-principles investigation, Surf. Sci. 664 (2017) 185–193.
[15] M.K. Agusta, M. David, H. Nakanishi, H. Kasai, Hydrazine (N2H4) adsorption on Ni (100): density functional theory investigation, Surf. Sci. 604 (2010) 245–251.
[16] P. Giannozzi, S. Baroni, N. Bonini, M. Calandra, R. Car, C. Cavazzoni, D. Ceresoli, G.L. Chiarotti, M. Cococcioni, I. Dabo, A. Dal Corso, S. de Gironcoli, S. Fabris, G. Fratesi, R. Gebauer, U. Gerstmann, C. Gougoussis, A. Kokalj, M. Lazzeri, L. Martin-Samos, N. Marzari, F. Mauri, R. Mazzarello, S. Paolini, A. Pasquarello, L. Paulatto, C. Sbraccia, S. Scandolo, G. Sclauzero, A.P. Seitsonen, A. Smogunov, P. Umari, R.M. Wentzcovitch, QUANTUM ESPRESSO: a modular and open-source software project for quantum simulations of materials, J. Phys. Condens. Matter 21 (2009) 395502.
[17] J. Perdew, K. Burke, M. Ernzerhof, Generalized gradient approximation made simple, Phys. Rev. Lett. 77 (1996) 3865–3868.
[18] G. Kresse, D. Joubert, From ultrasoft pseudopotentials to the projector augmented-wave method, Phys. Rev. B: Condens. Matter Mater. Phys. 59 (1999) 1758–1775.
[19] P.E. Blöchl, Projector augmented-wave method, Phys. Rev. B: Condens. Matter Mater. Phys. 50 (1994) 17953–17979.
[20] C.G. Broyden, The convergence of a class of double-rank minimization algorithms 1. General considerations, IMA J. Appl. Math. 6 (1970) 76–90.
[21] R. Fletcher, A new approach to variable metric algorithms, Comput. J. 13 (1970) 317–322.
[22] S. Grimme, J. Antony, S. Ehrlich, H. Krieg, A consistent and accurate ab initio parametrization of density functional dispersion correction (DFT-D) for the 94 elements H-Pu, J. Chem. Phys. 132 (2010) 154104.
[23] M.P. Andersson, Density functional theory with modified dispersion correction for metals applied to self-assembled monolayers of thiols on Au(111), J. Theor. Chem. 2013 (2013) 1–9.
[24] C. Kittel, Introduction to Solid State Physics, Wiley & Sons, Inc, 2004.
[25] O.I. Malyi, Z. Chen, V.V. Kulish, K. Bai, P. Wu, Density functional theory study of the effects of alloying additions on sulfur adsorption on nickel surfaces, J. Appl. Surf. Sci. 264 (2013) 320–328.
[26] G.W. Watson, E.T. Kelsey, N.H. de Leeuw, D.J. Harris, S.C. Parker, Atomistic simulation of dislocations, surfaces and interfaces in MgO, J. Chem. Soc. Faraday Trans. 92 (1996) 433–438.
[27] H.J. Monkhorst, J.D. Pack, Special points for Brillouin-zone integrations, Phys. Rev.

B 13 (1976) 5188.
[28] W.-B. Zhang, C. Chen, S.-Y. Zhang, Equilibrium crystal shape of Ni from first principles, J. Phys. Chem. C 117 (2013) 21274–21280.
[29] F. Mittendorfer, A. Eichler, J. Hafner, Structural, electronic and magnetic properties of nickel surfaces, Surf. Sci. 423 (1999) 1–11.
[30] L. Vitos, A.V. Ruban, H.L. Skriver, J. Kollar, The surface energy of metals, Surf. Sci. 411 (1998) 186–202.
[31] S. Hong, Y.-H. Shin, J. Ihm, Crystal shape of a nickel particle related to carbon nanotube growth, Jpn. J. Appl. Phys. 41 (2002) 6142.